Interface Reactions Dominate Low-Temperature CO Oxidation Activity over Pt/CeO<inf>2</inf>

THE JOURNAL OF PHYSICAL CHEMISTRY C
A JOURNAL OF THE AMERICAN CHEMICAL SOCIETY

pubs.acs.org/JPCC

Article

Interface Reactions Dominate Low-Temperature CO Oxidation Activity over Pt/CeO_2

Noemi Bosio,* Mengqiao Di, Magnus Skoglundh, Per-Anders Carlsson, and Henrik Grönbeck*

Cite This: *J. Phys. Chem. C* 2022, 126, 16164−16171

Read Online

ACCESS | Metrics & More | Article Recommendations | Supporting Information

ABSTRACT: First-principles-based kinetic Monte Carlo simulations and kinetic experiments are used to explore CO oxidation over Pt/CeO_2. The simulations compare CO oxidation over a ceria-supported ∼1 nm particle with simulations of a free-standing particle and Pt(111). The onset of the CO oxidation over ceria supported Pt is shifted to lower temperatures compared to the unsupported systems thanks to a Mars−van Krevelen mechanism at the Pt/CeO_2 interface perimeter, which is not sensitive to CO poisoning. Both the Mars−van Krevelen mechanism and the conventional Langmuir−Hinshelwood mechanism over the Pt nanoparticle are contributing to the conversion after the reaction onset. The reaction orders in CO and O_2 are compared experimentally for Pt/CeO_2 and Pt/Al_2O_3. The reaction orders over Pt/CeO_2 are close to zero for both CO and O_2, whereas the corresponding reaction orders are −0.75 and 0.68 over Pt/Al_2O_3. The measured zero orders for Pt/CeO_2 show the absence of CO/O_2 site competition and underline the relevance of interface reactions. The measurements for Pt/Al_2O_3 indicate that the main reaction path for CO oxidation over Pt is a conventional Langmuir−Hinshelwood reaction. The results elucidate the interplay between condition-dependent reaction mechanisms for CO oxidation over Pt supported on reducible oxides.

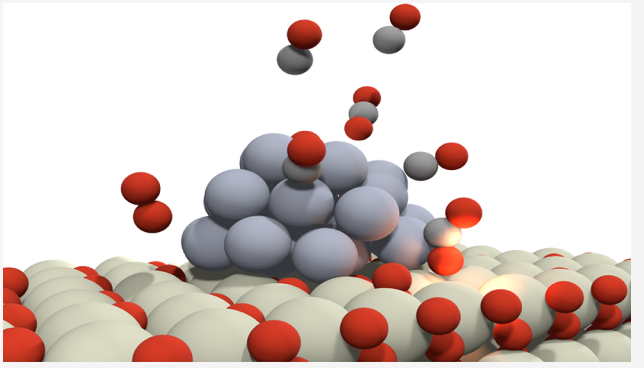

INTRODUCTION

Low-temperature CO oxidation continues to be a technologically critical reaction. One example is energy-efficient combustion, which results in cold exhaust streams calling for catalytic systems that are active in a wide temperature range. Commercial CO oxidation catalysts are based on supported precious-metal nanoparticles (NP), where Pt commonly is used as the active phase. However, the low-temperature activity of Pt is hindered by CO poisoning.[1] The poisoning originates from the difference in the number of sites required for CO and O_2 adsorption, the comparable adsorption energies, and the low sticking coefficient for O_2. The surface is at low temperatures covered in CO, which prevents dissociative adsorption of O_2. The onset of the reaction is determined by the CO desorption energy, and the reaction lights off when the adsorption−desorption equilibrium has a CO desorption rate that is high enough to allow for O_2 dissociation.[2]

Low-temperature oxidation can be accomplished by reducing the relative bond strength of CO with respect to O_2, which, for example, is the case for Au-based catalysts.[3] The drawback with Au-based catalysts is low activity at high temperatures, partly due to sintering of the active phase. Another strategy for low-temperature activity is to support Pt on a reducible support.[4] The suggestion is that the reaction on a reducible support can proceed via a Mars−van Krevelen mechanism[5] between CO adsorbed on the Pt and oxygen from the support, thus circumventing the site competition.

The different reaction mechanisms are sketched in Figure 1. Figure 1a represents the case with Pt supported on an irreducible oxide where the reaction proceeds on the Pt particle via the conventional Langmuir−Hinshelwood mechanism. It is commonly assumed that O_2 adsorbs dissociatively over Pt and that CO_2 is formed by reaction between CO and atomic oxygen.[6] The barrier for O_2 dissociation over Pt has been measured to be low, which indicates that dissociation is facile at temperatures when CO desorption is appreciable. The adsorption energy of CO_2 on metal surfaces is low, and the molecule is known to desorb once formed.[6,7] Figure 1b illustrates the reaction at the Pt/oxide interface at the particle interface perimeter for a reducible oxide. The assumption is that CO, which is adsorbed on Pt reacts with lattice oxygen in the oxide forming oxygen vacancies. The vacancies are replenished by direct O_2 adsorption forming a peroxide

Received: July 8, 2022
Revised: August 26, 2022
Published: September 14, 2022

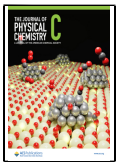

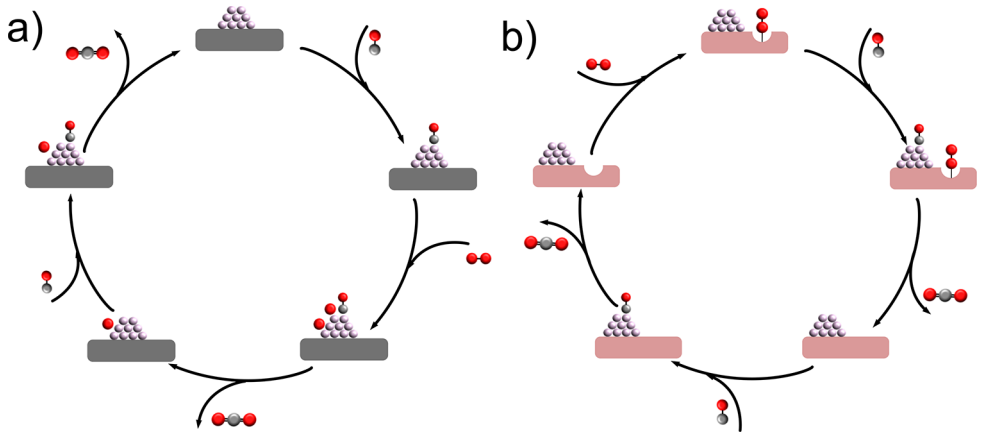

Figure 1. Steps during CO oxidation over a Pt particle supported on an irreducible oxide (a) and reducible oxide enabling interface reactions (b).

species. In a subsequent step, CO may react with the peroxide species, which closes the catalytic cycle.

The possibility of a perimeter reaction has clear consequences for the reaction kinetics. Assuming a low reaction rate and that CO is the most abundant reaction intermediate on Pt at low temperatures, the dependence of the reaction rate (r) on CO and O_2 partial pressures (p_{CO} and p_{O_2}) is given by

$$r \propto k_r \frac{\sqrt{K_{O_2} p_{O_2}}}{K_{CO} p_{CO}}$$

where K_{O_2} and K_{CO} are the equilibrium constants for O_2 and CO adsorption/desorption, respectively, and k_r is the (CO + O) reaction rate constant. Thus, the reaction orders are −1 and 0.5 for CO and O_2, respectively.[8] The situation is markedly different for the interface reaction, where CO and O_2 at low temperatures adsorb on different types of sites and the reaction can proceed via the Mars−van Krevelen mechanism. In the absence of site competition and facile O_2 adsorption, the reaction rate can be approximated by

$$r \simeq k_{r1}$$

where k_{r1} is the rate constant for the reaction between CO adsorbed on the metal phase and an oxygen anion in the oxide lattice. Thus, the interface reaction has reaction orders that are zero in both CO and O_2.

Ceria (CeO_2) is commonly added to technological catalysts as an oxygen buffer, and Pt supported on CeO_2 has previously been measured to show activity for CO oxidation at temperatures lower than for Pt supported on Al_2O_3.[4,9] However, the mechanism for the low-temperature activity is under debate, and the structure−function relation is still not clear. It has, for example, been suggested[10] that Pt-doped CeO_2 is responsible for the low-temperature activity for Pt supported on CeO_2. However, a recent experimental/computational study suggests that the onset of CO oxidation is connected to the formation of Pt clusters and that single Pt atoms are not active for the reaction.[11] One challenge when exploring structure/function relations for Pt particles supported on ceria is the structural flexibility where the particle size changes with reaction conditions.[12] Computationally, CO oxidation over Au/CeO_2 has been associated with high barriers,[13] and it has been suggested that doping of ceria is required for low-temperature activity.

One important aspect of catalysts based on ceria-supported metal particles is the strong metal−support interaction originating from a charge transfer between the metal and the support.[14] In the case of platinum supported on ceria, the charge transfer is in the direction from platinum to ceria.[15] As ceria is a reducible oxide, the charge transfer results in a change of the oxidation state of cerium cations from +4 in the stoichiometric oxide to +3 after the charge transfer. This suggests that ceria is in a reduced state, even in the absence of oxygen vacancies. The amount of charge that can be transferred from platinum to ceria depends on the size of the platinum nanoparticles. It has been shown through density functional theory calculations and X-ray photoemission spectroscopy that the amount of charge transferred increases with increased particle size until a certain limit is reached and the charge transferred per area reaches a plateau.[15] The largest charge transfer was measured for particles of ∼1.5 nm being about 0.1 electron per platinum atom.[15] Cerium cations in the +3 oxidation state are present also because of oxygen vacancies.[16] Thus, the presence of cerium cations in a +3 oxidation state can originate from both the metal−support interaction between Pt and ceria and oxygen vacancies. The reducible character of ceria with different charge transfer mechanisms convolutes the action of the Pt/ceria interface during CO oxidation.

Using a combination of density functional theory (DFT)-based kinetic Monte Carlo simulations and kinetic measurements, we are investigating CO oxidation over Pt/CeO_2 with the aim to clarify the role of the perimeter sites at the interface. The simulations indicate that low-temperature activity can be ascribed to the possibility of a Mars−van Krevelen reaction at the Pt/CeO_2 interface. The computational results are in accordance with the experiments, which reveal close to zero reaction orders in both CO and O_2 for CO oxidation over Pt/CeO_2, whereas the corresponding reaction orders are −0.75 (CO) and 0.68 (O_2) for comparative measurements over Pt/Al_2O_3.

EXPERIMENTAL AND COMPUTATIONAL METHODS

Light-Off and Reaction Order Measurements. The reaction order measurements are performed in a vertical fixed-bed powder reactor described elsewhere.[17] The effluent gas is detected by a Fourier transform infrared spectrometer (MKS MultiGas 2030 FTIR). The catalyst sample is sieved, and the

https://doi.org/10.1021/acs.jpcc.2c04833
J. Phys. Chem. C 2022, 126, 16164−16171

grain fraction with 40−80 μm is collected and diluted with cordierite (Corning) ground to 300−355 μm before it is loaded into the reactor. The catalyst weight is around 6 mg, and the catalyst-to-cordierite mass ratio is 1:30. The total gas flow is 400 mL/min, corresponding to a gas hourly space velocity of 127000 h^{-1}. Prior to the O_2 reaction order measurements, the catalysts are pretreated with 0.05 kPa of CO and 0.03 kPa of O_2 at 250 °C and thereafter cooled to 30 °C and exposed to 0.05 kPa of CO for 2 h prior to the measurements of the O_2 reaction order. The O_2 reaction order for the Pt/ceria catalyst is measured when feeding 0.05 kPa of CO and stepwise increase the O_2 pressure from 0.03 to 0.37 kPa at 125 °C. Each step is held for 1 h to reach steady state. The O_2 reaction order of Pt/alumina is measured with 0.05 kPa of CO in the O_2 range from 0.63 to 1.11 kPa at 145 °C. In the measurements of the CO reaction orders, the Pt/ceria catalyst is pretreated with 0.05 kPa of CO and 2 kPa of O_2 at 250 °C for 50 min; then the temperature is lowered to 125 °C, and the catalyst is exposed to a stepwise increase of CO pressure from 0.05 to 0.28 kPa with 2 kPa of O_2. For the Pt/alumina catalyst, the CO pressure varied from 0.14 to 0.34 kPa with 2 kPa of O_2 at 145 °C, and each step is maintained for 30 min with Ar as carrier gas throughout the measurements.

The catalyst performance is evaluated by using the reactor described above, and the effluent gas is analyzed by using a mass spectrometer (Hiden HPR-20) monitoring the m/e ratios 28 (CO), 32 (O_2), and 44 (CO_2). The CO oxidation measurements are performed using either 0.5, 0.2, or 0.05 kPa of CO with 2 kPa of O_2. Prior to the measurements, the catalysts are pretreated at 250 °C for 50 min. The measurements are performed with a temperature cycle repeated three times: the temperature is lowered to 50 °C and thereafter increased to 250 °C with a ramp rate of 5 °C/min.

Density Functional Theory (DFT) Calculations. Spin-polarized DFT calculations are performed with the Vienna Ab-initio simulation package (VASP).[18−20] The valence electrons are described with a plane wave basis set using a cutoff energy of 450 eV, whereas the interaction between the valence and the core electrons is described with the projector augmented wave (PAW) method.[21] The numbers of valence electrons treated explicitly in the calculations are C (4), O (6), Pt (10), and Ce (12). Exchange-correlation effects are modeled by using the Perdew−Burke−Ernzerhof (PBE) functional.[22] A Hubbard-U term[23] is used for Ce 4f to describe electron localization and formation of Ce^{3+} ions in the case of oxygen vacancies and charge transfer from Pt. Following the literature, a U value of 4.5 eV is used for Ce.[24] The k-point sampling is restricted to the gamma point. The electronic structure is considered to be converged when the energy difference between subsequent steps is smaller than 10^{-6} eV. The atomic geometries are optimized by using the conjugate gradient method, and the structures are considered to be converged when all forces are smaller than 10^{-2} eV/Å. The climbing image nudged elastic band (CI-NEB) method[25,26] is employed to calculate transition state structures and reaction barriers.

The applied exchange-correlation functional is known to overestimate the CO adsorption energy on Pt and suggest a preference for hollow adsorption on Pt(111), whereas atop adsorption is measured experimentally.[27] Because of the deficiencies, we have applied a correction to the CO adsorption energy as suggested by Abild-Pedersen and Andersson,[28] which yields the correct adsorption site and an adsorption strength in reasonable agreement with experiments.

Kinetic Monte Carlo Simulations. Kinetic Monte Carlo simulations are performed within the first reaction method[29] as implemented in ref 30. All the considered events are stored in an event list. Given two states of the system α and β, the time of occurrence for an event connecting α and β is in the first reaction method given by

$$t_{\beta\alpha} = t - \frac{1}{W_{\beta\alpha}}\ln(\rho) \tag{1}$$

where t is the current simulation time, $W_{\beta\alpha}$ is the reaction rate constant, and ρ is a uniform random number on the unit interval. If an event is enabled, the first process in the list is executed, the event list is updated, and the current simulation time is updated to the occurrence time.

For adsorption steps, the rate constant is calculated from collision theory:

$$W_{i,j}^{\mathrm{ads}} = \frac{s_{i,j}^{0} p_i A}{\sqrt{2\pi M_i k_B T}} \tag{2}$$

Here i is the type of reactant, j is the site index, p_i is the partial pressure, A is the area of the adsorption site, M_i is the mass of the gas-phase molecule, k_B is the Boltzmann constant, T is the temperature, and $s_{i,j}^{0}$ is a sticking coefficient accounting for the case that all molecules that hit the surface do not stick. The values for the sticking coefficients are set to 0.9 for CO and 0.1 for O_2 according to ref 31.

The desorption rate constants are connected to the rate constant for adsorption via the equilibrium constant $K_{i,j}$:

$$W_{i,j}^{\mathrm{des}} = \frac{W_{i,j}^{\mathrm{ads}}}{K_{i,j}}$$

which makes the model thermodynamically consistent. The equilibrium constant is given by

$$K_{i,j} = \exp\left[\frac{-E_{i,j}^{\mathrm{ads}} + T(S_i^{\mathrm{ads}} - S_i^{\mathrm{g}})}{k_B T}\right]$$

$E_{i,j}^{\mathrm{ads}}$ is the adsorption energy of reactant i on site j. S_i^{gas} and S_i^{ads} are the entropies of the species in gas phase and adsorbed phase, respectively. The entropies of the adsorbed species are calculated in the harmonic approximation.[32]

The rate constant for the CO oxidation reaction at site j is evaluated by transition state theory:[33]

$$W_j = \frac{k_B T}{h}\left(\frac{Z^{\mathrm{TS}}}{Z^{\mathrm{IS}}}\right)\exp\left(\frac{-E_j}{k_B T}\right)$$

where Z^{TS} and Z^{IS} are the partition functions for the transition and initial state, respectively, and E_j is the reaction barrier. The partition function of the transition state (Z^{TS}) does not include the reaction coordinate, which is included in the term $k_B T/h$.

Active sites on the nanoparticle are considered as coarse-grained sites; thus, the distinct geometrical adsorption sites (atop, fcc, bridge, and hcp) are merged. A neighbors list is constructed, which defines the site connectivity and which events that are possible. The reaction is simulated in the temperature range −100 to 500 °C. For statistical accuracy, ten simulations are run for each temperature, and the average is taken. The convergence of turnover frequency (TOF) and coverage with respect to time is monitored to ensure that steady state has been reached.

https://doi.org/10.1021/acs.jpcc.2c04833
J. Phys. Chem. C 2022, 126, 16164−16171

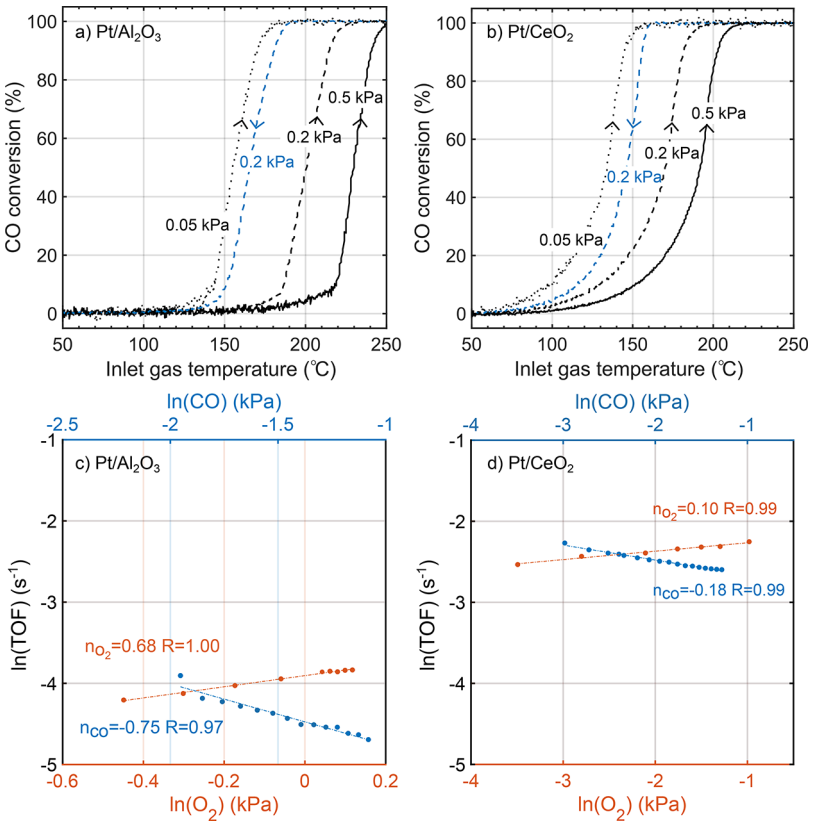

Figure 2. (a, b) Temperature-dependent CO conversion for Pt/Al_2O_3 and Pt/CeO_2 at 0.05, 0.2 and 0.5 kPa of CO and 2 kPa O_2. (c, d) Measured pressure dependencies of the turnover frequency for Pt/Al_2O_3 and Pt/CeO_2. The reaction orders are obtained by linear fitting. The measurements are performed at 145 and 125 °C for Pt/Al_2O_3 and Pt/CeO_2, respectively.

RESULTS AND DISCUSSION

Light-Off Experiments and Reaction Orders. The temperature dependence of the CO conversion and reaction orders are shown in Figure 2. The results for Pt/CeO_2 are compared to Pt/Al_2O_3, thus comparing ceria with an irreducible oxide. From the temperature dependence, it is evident that the Pt/CeO_2 system shows activity at lower temperatures than the Pt/Al_2O_3 system for all investigated pressures (0.05, 0.2, and 0.5 kPa of CO and 2 kPa of O_2). Defining the light-off temperature as the temperature where the conversion is 10% of the maximum conversion, the light-off temperature for the Pt/Al_2O_3 system varies from around 130 to 200 °C. The light-off temperature has a clear pressure dependence where the lowest temperature is measured for the case with a CO pressure of 0.05 kPa. The light-off temperature for Pt/CeO_2 is well below 150 °C for all investigated pressures. Moreover, the temperature dependencies of the conversions show different characteristics; whereas a sharp and sudden increase in the conversion is measured for the Pt/Al_2O_3 system, the conversion increases exponentially for Pt/CeO_2. The reaction shows bistability and we include also the extinction results for the case of a CO pressure of 0.2 kPa.[17] The bistability window is about 40 and 25 °C for Pt/Al_2O_3 and Pt/CeO_2, respectively.

The reaction is characterized by measurements of the reaction orders. The reaction orders are measured around pressures of 0.05 kPa for CO and 2 kPa for O_2. In the case of Pt/Al_2O_3, the CO reaction order at 145 °C is measured to be −0.75, whereas the reaction order in oxygen is measured to be +0.68. For Pt/CeO_2, the reaction orders are at 125 °C measured to be −0.18 and +0.1 for CO and O_2, respectively. The temperatures to measure the reaction orders are chosen to measure for conversions lower than 22%.

Model Systems and Evaluation of Kinetic Parameters. Computational model systems are constructed to obtain adsorption energies and reaction energies. The experimental systems are generally structurally ill-defined; however, scanning transmission electron microscopy measurements of technical catalysts have revealed Pt nanoparticles supported on the $CeO_2(111)$ facet.[34] $CeO_2(111)$ is the stable ceria surface, and we consider Pt supported on this surface.

To model a supported Pt particle in the nanometer range, we investigate Pt_{34} in the form of a truncated octahedron (see Figure 3a,b). The diameter of Pt_{34} is about 0.8 nm and comparable with the experimental average value, which has been measured to be 1 nm.[17] The particle exposes a Pt(100) microfacet to the oxide support. $CeO_2(111)$ is constructed with five O−Ce−O trilayers. The structurally relaxed particle is distorted with respect to the original octahedral structure. The distortion can be attributed to both the corrugated potential energy surface of the CeO_2 and the fact that the truncated octahedron is not the global energy minimum of the structure. CO and O adsorption energies are calculated for the different sites along the perimeter of the supported particle. CO is initially placed in atop positions and structurally optimized to the closest minimum, whereas atomic oxygen is initially placed in bridge positions. The adsorption energies with respect to gas phase CO and O_2 are found to have a wide spread. The CO adsorption energies range from −1.50 to −2.30 eV, whereas the oxygen adsorption energy (per atom) ranges from −0.68 to

https://doi.org/10.1021/acs.jpcc.2c04833
J. Phys. Chem. C 2022, 126, 16164−16171

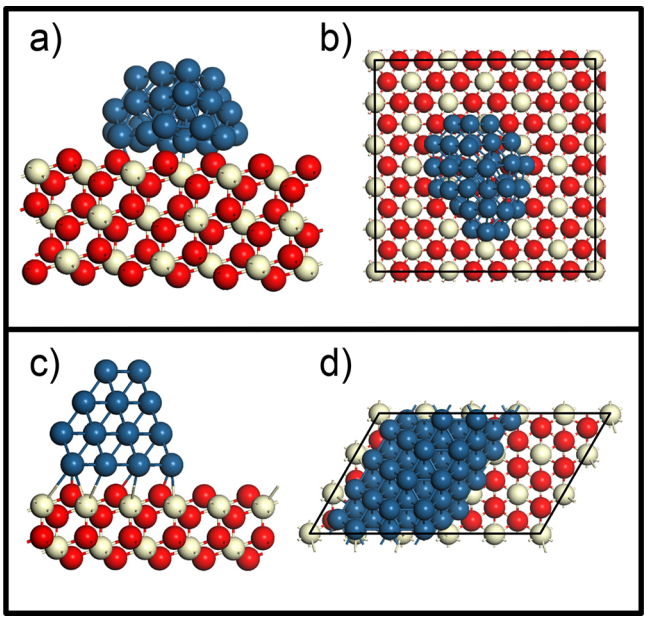

Figure 3. (a) Side and (b) top view of a Pt_{34} particle supported on a three-layer $CeO_2(111)$. The ceria surface is modeled by using a rectangular $(5 \times 3\sqrt{3})$ surface cell (indicated). (c) Side and (d) top view of a 32-atom Pt rod on $CeO_2(111)$. The rod is modeled on the $CeO_2(111)$ surface by using a (3×5) surface cell (indicated) with two trilayers. Atomic color codes: red (O), blue (Pt), and beige (Ce).

−1.50 eV. The values could be compared to the corresponding values for Pt(111), which are calculated to be −1.42 and −1.22 eV for CO and O, respectively. The energy for oxygen is calculated with respect to O_2 in the gas phase. A detailed account of the adsorption energies is given in the Supporting Information.

The reaction barrier on the Pt phase is calculated from a Brønsted−Evans−Polanyi relation.[35,36] The barrier (in eV) is given by

$$E_a = 0.92 + 0.18(\Delta E_{CO} + \Delta E_O) \quad (3)$$

where 0.92 corresponds to the barrier calculated on a clean Pt(111) surface and ΔE_{CO} and ΔE_O are the changes of the CO and O adsorption energies with respect to the values on the extended (111) surface. Adsorbate−adsorbate interactions are treated as in ref 36.

A rod model is used to estimate the barriers for CO oxidation at the interface (see Figure 3c,d). The rod model consists of 32 Pt atoms and exposes a Pt(111) surface to the $CeO_2(111)$ surface, which is modeled with two trilayers. In the pristine system, different configurations have been investigated, corresponding to different amounts of charge transfer from the platinum rod to the ceria support. Configurations with one to three electrons transferred from platinum to ceria have been found with similar energies, which corresponds to a fraction of 6−10% Ce^{3+} ions, which agrees with the literature.[15] The oxygen vacancy formation energy in $CeO_2(111)$ is for the rod system calculated to be 1.92 eV, which could be compared to 2.01 eV for the surface cell in the absence of the rod and 2.16 eV for the bare $CeO_2(111)$ surface in a $(2\sqrt{3} \times 5)$ surface cell with five trilayers. The excess charge in the case of the vacancy is localized in ceria forming two Ce^{3+} ions. Thus, it is energetically favorable to change the oxidation state of Ce instead of delocalizing the charge in the Pt rod, which is expected given the spontaneous metal-to-oxide charge transfer. The total amount of Ce^{3+} ions is two in the case of the model rod system with an oxygen vacancy.

One of the challenges when calculating the CO oxidation barrier at the interface resides in the transfer and localization of the charge. Ce^{3+} ions are formed in the system both via the intrinsic platinum to ceria charge transfer and upon the formation of vacancies. Because of the limited amount of Ce^{3+} ions that the surface cell can accommodate, the reaction at the interface where an oxygen vacancy is formed may not always result in additional Ce^{3+} ions. Because of the two charge transfer mechanisms, the calculation of energy barriers with NEB calculations proved to be challenging. The main difficulty is the difference in charge transfer between ceria atoms and the platinum rod along the reaction path. We performed multiple NEB calculations; however, due to convergence issues, we have not been able to confirm the transition states by vibrational analysis. Nevertheless, all calculations resulted in similar estimates for the transition states structure and for the energy barrier, resulting in a barrier between 0.9 and 1.0 eV for the reaction between CO and a lattice oxygen and a barrier between 0.3 and 0.4 eV for the reaction between CO and O_2 adsorbed in an oxygen vacancy.

Figure 4 shows the potential energy diagram for the reaction at the Pt rod interface to $CeO_2(111)$. The reaction is

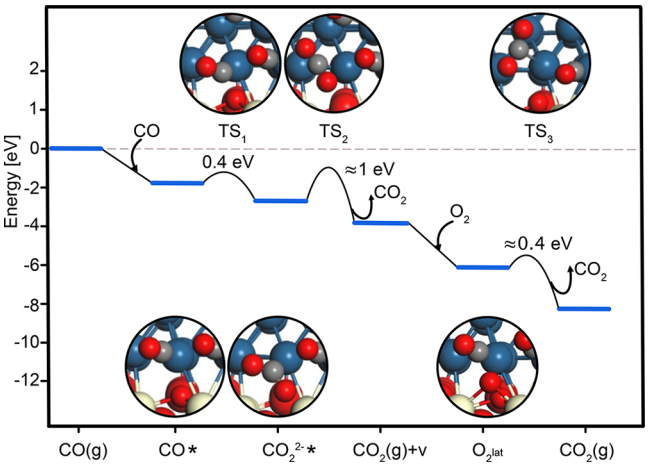

Figure 4. Potential energy landscape for CO oxidation over Pt/CeO_2. Atomic color code as in Figure 3 with gray (C).

considered in the high coverage limit with a CO coverage of 0.7 (10 CO molecules). The catalytic cycle starts with the formation of an oxygen vacancy via reaction between CO at the Pt and an oxygen anion in the ceria surface. An oxygen anion close to the rod is initially perturbed in the direction of the CO molecule forming a CO_2^{2-} species (TS_1) at the interface with a small barrier of ∼0.4 eV. The charge state is confirmed with a Bader analysis and the O−C−O angle, which is 118°. The barrier (TS_2) for desorption of CO_2 to the gas-phase is calculated to be ≃1.0 eV. Thus, the highest barrier along the reaction path is the desorption of CO_2. This is in variance with the situation on a pure Pt system, where the desorption energy of CO_2 is low. Once the vacancy is formed, O_2 can adsorb in the vacancy forming a peroxide species with an O−O bond of 1.44 Å. The adsorption energy of O_2 in a vacancy is −1.93 eV. The catalytic cycle is completed by CO

https://doi.org/10.1021/acs.jpcc.2c04833
J. Phys. Chem. C 2022, 126, 16164−16171

reacting with the peroxide species (TS_3). The reaction has a small barrier of ≃0.4 eV and is exothermic by −2.67 eV.

The number of Ce^{3+} cations in the system does not change during the reaction. Two Ce^{3+} cations are present in the initial, intermediate, and final state. Thus, the creation of the O vacancy does not result in additional Ce^{3+} ions.

Kinetic Monte Carlo Simulations. Having the adsorption energies of CO and O and an estimate for the barriers for CO oxidation at the interface perimeter, we use kinetic Monte Carlo simulations to simulate the reaction kinetics. The considered reactions are

$$CO(g) + * \leftrightarrow CO* \quad (R1)$$

$$CO* + * \leftrightarrow * + CO* \quad (R2)$$

$$O_2(g) + 2* \leftrightarrow 2O* \quad (R3)$$

$$O* + * \leftrightarrow * + O* \quad (R4)$$

$$CO* + O* \rightarrow CO_2(g) + 2* \quad (R5)$$

$$CO* + O_{lat} \rightarrow CO_2(g) + v \quad (R6)$$

$$O_2(g) + v \rightarrow (O_2)_{lat} \quad (R7)$$

$$CO* + (O_2)_{lat} \rightarrow CO_2(g) + O_{lat} + * \quad (R8)$$

Reactions R1−R5 represent the reactions on the Pt phase of the catalyst. (R1) is adsorption and desorption of CO, (R2) is diffusion of CO, (R3) is the forward and backward reaction of dissociative adsorption of O_2, and (R4) is O diffusion. (R5) is CO_2 formation from adsorbed CO and O. Steps (R6), (R7), and (R8) are the reaction steps at the interface. (R6) is the formation of CO_2 from CO adsorbed on Pt and an oxygen atom in the $CeO_2(111)$ surface (O_{lat}), resulting in an oxygen vacancy in the oxide (v). Here we treat the formation of CO_2^{2-} at the interface and the desorption of CO_2 as one lumped reaction step. (R7) is the molecular adsorption of O_2 in the vacancy site. (R8) is the formation of CO_2 from CO at the Pt phase and molecular oxygen adsorbed in the vacancy. As effective barriers for (R6) and (R8), we use 0.92 and 0.40 eV, respectively. CO and O_2 adsorption on $CeO_2(111)$ is not included in the reaction scheme as the adsorption energies are too low to yield an appreciable coverage at temperatures relevant for the reaction. Moreover, diffusion of oxygen vacancies in $CeO_2(111)$ is not considered as the Mars−van Krevelen reaction path is limited by the formation of a vacancy at the Pt/CeO_2 interface.

The turnover frequencies (TOF) over Pt(111) and ceria-supported Pt_{34} are shown in Figure 5. The simulations are performed with pressures of 0.2 and 2 kPa for CO and O_2, respectively. The standard deviations of the TOF in the simulations are small [$<1\ s^{-1}$ at 100 °C for both Pt(111) and $Pt_{34}/CeO_2(111)$]. The reaction over Pt(111) follows our previous results.[37] CO poisons the surface at low temperatures, and the TOF increases after 125 °C. The TOF for a free-standing Pt_{34} cluster is shown in Figure 5b. The onset of the TOF is for Pt_{34} shifted to higher temperatures, i.e., 175 °C. The delayed onset of the reaction is due to the stronger adsorption energies of CO on the cluster as compared to the Pt(111) surface. Thus, the intrinsic low-temperature activity of the metal phase of the model system is lower than for Pt(111), which is in agreement with previous Sabatier simulations.[38]

The situation is markedly different for Pt supported on $CeO_2(111)$ shown in Figure 5c. This system has an increase in

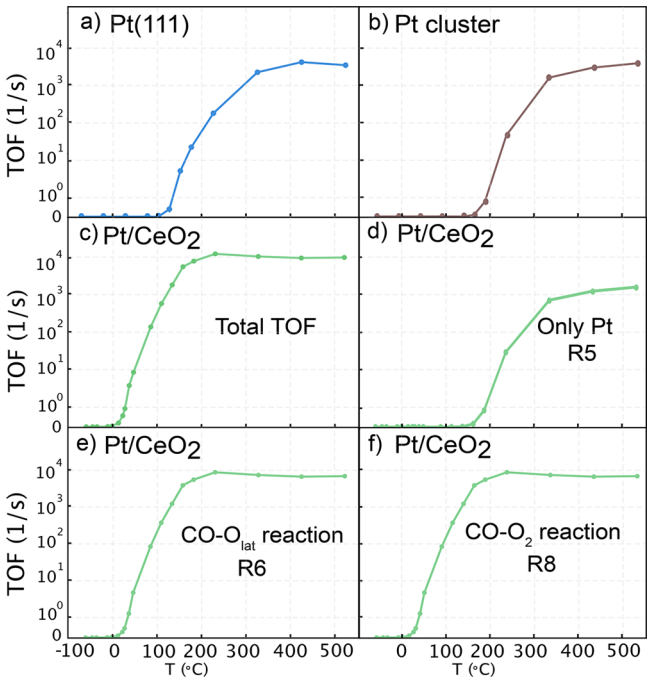

Figure 5. (a) Total TOF for CO oxidation over Pt(111). (b) TOF for CO oxidation over a free-standing Pt_{34} particle. (c) TOF over ceria supported Pt_{34}. (d−f) Decovolution of the reaction paths contributing to the total TOF over ceria-supported Pt_{34}. The simulations are performed at CO and O_2 partial pressures of 0.2 and 2 kPa, respectively.

the TOF at ∼0 °C, which is about 125 °C lower than the one obtained for Pt(111). The kinetic behavior at high temperatures is qualitatively similar to the one obtained for CO oxidation over larger Pt nanoparticles.[37] The TOF for the supported particle is deconvoluted in Figure 5d−f. In Figure 5d, only the contribution from the reaction between CO and O adsorbed on Pt (R5) is shown, having a temperature dependence similar to that on the Pt_{34} particle (Figure 5b). Figure 5e,f shows the contributions to the TOF from the perimeter sites. The two contributions are similar, which is a consequence of the fact that (R6) controls the rate, as the barrier for CO_2 formation from adsorbed O_2 is low.

The simulations show that the onset of the reaction of the Pt particle is lowered by ∼175 °C when it is supported by ceria. In the experiments (Figure 2), the difference in light-off between the ceria and alumina supported particles is ∼70 °C. In general, the simulated onsets of the TOF are lower than the corresponding experimental temperatures, which reflects the uncertainty in the DFT energies. It should be noted that the reaction shows a bistability where the light-off temperature is higher than the extinction temperature. The difference arises as the platinum phase is covered by CO as the temperature is increased, whereas the coverage is low as the temperature is decreased. The simulations were performed by initializing the system with a bare surface, yielding a situation close to the ignition conditions.

The simulations for the supported Pt_{34} particle show that the Mars−van Krevelen steps control the reaction. The effective barrier for CO_2 formation is not substantially lower at the $Pt/CeO_2(111)$ interface than on Pt(111). However, the possibility of the interface reaction provides a possibility to circumvent the CO poisoning.

https://doi.org/10.1021/acs.jpcc.2c04833
J. Phys. Chem. C 2022, 126, 16164−16171

It is clear that onset of the reaction is controlled by the reaction energies. For bare Pt, it is the desorption energy of CO (including the adsorbate−adsorbate interactions) that control the light-off, whereas for CeO_2-supported Pt, it is the barrier for the interface reaction R6 that controls the light-off. The barrier for the interface reaction depends on the oxygen vacancy formation energy, which is affected by the detailed structure and chosen exchange-correlation functional.

Additional simulations are performed to calculate the apparent activation energy of the reaction. Because of the uncertainty of the barrier at the interface, we performed simulations for cases where the (R6) barrier also is modified with respect to the computed estimate. The simulations are performed for pressures P_{CO} = 0.5 kPa and P_{O_2} = 2 kPa (lean conditions) and P_{CO} = 0.5 kPa and P_{O_2} = 0.3 kPa (rich conditions). The results are summarized in Table 1.

Table 1. Apparent Activation Energy for CO Oxidation over Pt/CeO_2 for Different Values of the (R6) Barrier[a]

ΔE_{CO+O_i}	E_{app}(lean)	E_{app}(rich)
0.70	0.51	0.43
0.92	0.77	0.72
1.20	1.20	1.11
temp direction	E_{app}(lean)	E_{app}(rich)
ignition	0.53 ± 0.02	0.43 ± 0.02
extinction	0.62 ± 0.02	0.70 ± 0.08

[a]The simulations are performed for lean (p_{CO} = 0.5 kPa, p_{O_2} = 2 kPa) and rich (p_{CO} = 0.5 kPa, p_{O_2} = 0.3 kPa) conditions. The simulations are compared to experimental values analyzed for ignition and extinction.

The simulated apparent activation energies show a difference of about 0.1 eV between simulations performed for the lean and rich conditions. This is in good agreement with the experiments. The apparent activation energy for an (R6) barrier of 0.70 eV is close to the experimental results for ignition, which match the simulated conditions (the surface is initialized with zero coverages). The apparent activation energy is sensitive to the (R6) barrier. An increased (R6) barrier yields an increased apparent activation energy. When the barrier is higher than the barrier for CO oxidation on platinum, the apparent activation energy is similar to the values obtained for the unsupported platinum cluster. For the unsupported cluster, we obtain apparent activation energies of 1.20 and 1.23 eV for lean and rich conditions, respectively. The high apparent activation energy reflects that the reaction proceeds mainly on the platinum cluster. Previous experiments have reported similar apparent activation energies for CO oxidation over Pt/CeO_2. Taking the example of ignition in lean conditions and Pt particles smaller than 5 nm, refs 39 and 40 report 0.57 and 0.69 eV, respectively.

CONCLUSION

Using a combination of first-principles based kinetic Monte Carlo simulations and kinetic measurements, we have investigated CO oxidation over ceria supported Pt and compared the results with alumina supported Pt. Pt supported on ceria is found to have a higher low-temperature activity than Pt supported on alumina. The simulations indicate that the enhanced low-temperature activity of Pt/CeO_2 is enabled by a Mars−van Krevelen reaction at the Pt/CeO_2 interface. The Mars−van Krevelen reaction is found to proceed in two steps with a low barrier for the formation of a CO_2^{2-} species at the interface and a rate-determining barrier for CO_2 desorption. By deconvoluting the contributions from the different reaction steps, we show that the Mars−van Krevelen path dominates the activity at low temperatures. Moreover, the contribution from the conventional Langmuir−Hinshelwood reaction over the Pt particle is not affected by the ceria support and shows an activity similar to a free-standing particle. The intrinsic activity of the free-standing Pt particle is found to be lower than that of Pt(111), which suggests that the activity for CO oxidation over ceria supported Pt is strongly affected by the support. The computational results are in accordance with the experiments revealing close to zero reaction orders for CO and O_2 during oxidation over Pt/CeO_2, whereas the corresponding reaction orders are −0.75 and 0.68 for Pt/Al_2O_3. The results elucidate the effects of reactions at interfaces and the active sites for Pt supported on reducible oxides.

ASSOCIATED CONTENT

Supporting Information

The Supporting Information is available free of charge at https://pubs.acs.org/doi/10.1021/acs.jpcc.2c04833.

Calculated adsorption energies on the Pt_{34} particle and structures for the transition states (PDF)

AUTHOR INFORMATION

Corresponding Authors

Noemi Bosio − *Department of Physics and Competence Centre for Catalysis, Chalmers University of Technology, SE-412 96 Göteborg, Sweden*; Email: bosio@chalmers.se

Henrik Grönbeck − *Department of Physics and Competence Centre for Catalysis, Chalmers University of Technology, SE-412 96 Göteborg, Sweden*; orcid.org/0000-0002-8709-2889; Email: ghj@chalmers.se

Authors

Mengqiao Di − *Department of Chemistry and Chemical Engineering and Competence Centre for Catalysis, Chalmers University of Technology, SE-412 96 Göteborg, Sweden*

Magnus Skoglundh − *Department of Chemistry and Chemical Engineering and Competence Centre for Catalysis, Chalmers University of Technology, SE-412 96 Göteborg, Sweden*; orcid.org/0000-0001-7946-7137

Per-Anders Carlsson − *Department of Chemistry and Chemical Engineering and Competence Centre for Catalysis, Chalmers University of Technology, SE-412 96 Göteborg, Sweden*; orcid.org/0000-0001-6318-7966

Complete contact information is available at: https://pubs.acs.org/10.1021/acs.jpcc.2c04833

Notes

The authors declare no competing financial interest.

ACKNOWLEDGMENTS

The Competence Centre for Catalysis (KCK) is hosted by Chalmers University of Technology and financially supported by the Swedish Energy Agency (52689-1) and the member companies Johnson Matthey, Perstorp, Powercell, Preem, Scania CV, Umicore, and Volvo Group. Support from the Swedish Research Council (2020-05191) is acknowledged.

The calculations have been performed at C3SE (Göteborg) through a SNIC grant.

REFERENCES

(1) van Spronsen, M. A.; Frenken, J. W. M.; Groot, I. M. N. Surface science under reaction conditions: CO oxidation on Pt and Pd model catalysts. *Chem. Soc. Rev.* **2017**, *46*, 4347−4374.

(2) Freund, H.-J.; Meijer, G.; Scheffler, M.; Schlogl, R.; Wolf, M. CO oxidation as a prototypical reaction for heterogeneous processes. *Angew. Chem., Int. Ed.* **2011**, *50*, 10064−10094.

(3) Haruta, M.; Yamada, N.; Kobayashi, T.; Iijima, S. Gold catalysts prepared by coprecipitation for low-temperature oxidation of hydrogen and of carbon monoxide. *J. Catal.* **1989**, *115*, 301−309.

(4) An, K.; Alayoglu, S.; Musselwhite, N.; Plamthottam, S.; Melaet, G.; Lindeman, A. E.; Somorjai, G. A. Enhanced CO oxidation rates at the interface of mesoporous oxides and Pt nanoparticles. *J. Am. Chem. Soc.* **2013**, *135*, 16689−16696.

(5) Doornkamp, C.; Ponec, V. The universal character of the Mars and Van Krevelen mechanism. *J. Mol. Catal. A: Chemical* **2000**, *162*, 19−32.

(6) Campbell, C. T.; Ertl, G.; Kuipers, H.; Segner, J. A molecular beam investigation of the interactions of CO with a Pt(111) surface. *Surf. Sci.* **1981**, *107*, 207−219.

(7) Engel, T.; Ertl, G. A molecular beam investigation of the catalytic oxidation of CO on Pd(111). *J. Chem. Phys.* **1978**, *69*, 1267.

(8) Chorkendorff, I.; Niemantsverdriet, J. W. *Concepts of Modern Catalysis and Kinetics*; John Wiley & Sons: Weinheim Germany, 2017.

(9) Carlsson, P.-A.; Skoglundh, M. Low-temperature oxidation of carbon monoxide and methane over alumina and ceria supported platinum catalysts. *Appl. Catal. B: Environ.* **2011**, *101*, 669−675.

(10) Nie, L.; Mei, D.; Xiong, H.; Peng, B.; Ren, Z.; Hernandez, X. I. P.; DeLaRiva, A.; Wang, M.; Engelhard, M. H.; Kovarik, L.; Datye, A. K.; Wang, Y. Activation of surface lattice oxygen in single-atom Pt/CeO_2 for low-temperature CO oxidation. *Science* **2017**, *358*, 1419.

(11) Maurer, F.; Jelic, J.; Wang, J.; Gänzler, A.; Dolcet, P.; Wöll, C.; Wang, Y.; Studt, F.; Casapu, M.; Grunwaldt, J.-D. Tracking the formation, fate and consequence for catalytic activity of Pt single sites on CeO_2. *Nat. Catal.* **2020**, *3*, 824−833.

(12) Wang, J.; Sauter, E.; Nefedov, A.; Heissler, S.; Maurer, F.; Casapu, M.; Grunwaldt, J.-D.; Wang, Y.; Wöll, C. Dynamic Structural Evolution of Ceria-Supported Pt Particles: A Thorough Spectroscopic Study. *J. Phys. Chem. C* **2022**, *126*, 9051−9058.

(13) Kim, H. Y.; Henkelman, G. CO oxidation at the interface between doped CeO_2 and supported Au nanoclusters. *J. Phys. Chem. Lett.* **2012**, *3*, 2194−2199.

(14) Campbell, C. T. Catalyst-support interactions: Electronic perturbations. *Nat. Chem.* **2012**, *4*, 597−598.

(15) Lykhach, Y.; et al. Counting electrons on supported nanoparticles. *Nat. Mater.* **2016**, *15*, 284−288.

(16) Murgida, G. E.; Ferrari, V.; Ganduglia-Pirovano, M. V.; Llois, A. M. Ordering of oxygen vacancies and excess charge localization in bulk ceria: A DFT + *U* study. *Phys. Rev. B* **2014**, *90*, 115120.

(17) Di, M.; Simmance, K.; Schaefer, A.; Feng, Y.; Hemmingsson, F.; Skoglundh, M.; Bell, T.; Thompsett, D.; Ajakaiye Jensen, L. I.; Blomberg, S.; Carlsson, P.-A. Chasing PtO_x species in ceria supported platinum during CO oxidation extinction with correlative operando spectroscopic techniques. *J. Catal.* **2022**, *409*, 1−11.

(18) Kresse, G.; Furthmüller, J. Efficient iterative schemes for ab initio total-energy calculations using a plane-wave basis set. *Phys. Rev. B* **1996**, *54*, 11169−11186.

(19) Kresse, G.; Furthmüller, J. Efficiency of ab-initio total energy calculations for metals and semiconductors using a plane-wave basis set. *Comput. Mater. Sci.* **1996**, *6*, 15−50.

(20) Kresse, G.; Hafner, J. Ab initio molecular dynamics for liquid metals. *Phys. Rev. B* **1993**, *47*, 558−561.

(21) Blöchl, P. E. Projector augmented-wave method. *Phys. Rev. B* **1994**, *50*, 17953−17979.

(22) Perdew, J.; Burke, K.; Ernzerhof, M. Generalized gradient approximation made simple. *Phys. Rev. Lett.* **1996**, *77*, 3865−3868.

(23) Anisimov, V. I.; Zaanen, J.; Andersen, O. K. Band theory and Mott insulators: Hubbard U instead of Stoner I. *Phys. Rev. B* **1991**, *44*, 943−954.

(24) Huang, M.; Fabris, S. CO adsorption and oxidation on ceria surfaces from DFT+U calculations. *J. Phys. Chem. C* **2008**, *112*, 8643−8648.

(25) Mills, G.; Jónsson, H.; Schenter, G. K. Reversible work transition state theory: application to dissociative adsorption of hydrogen. *Surf. Sci.* **1995**, *324*, 305−337.

(26) Henkelman, G.; Uberuaga, B. P.; Jónsson, H. Climbing image nudged elastic band method for finding saddle points and minimum energy paths. *J. Chem. Phys.* **2000**, *113*, 9901−9904.

(27) Feibelman, P. J.; Hammer, B.; Nørskov, J. K.; Wagner, F.; Scheffler, M.; Stumpf, R.; Watwe, R.; Dumesic, J. The CO/Pt(111) Puzzle. *J. Phys. Chem. B* **2001**, *105*, 4018−4025.

(28) Abild-Pedersen, F.; Andersson, M. P. CO adsorption energies on metals with correction for high coordination adsorption sites − A density functional study. *Surf. Sci.* **2007**, *601*, 1747−1753.

(29) Jansen, A. P. J. *An Introduction to Monte Carlo Simulations of Surface Reactions*; Springer-Verlag: Berlin, 2003.

(30) Jørgensen, M.; Grönbeck, H. MonteCoffee: A programmable kinetic Monte Carlo framework. *J. Chem. Phys.* **2018**, *149*, 114101.

(31) Vogel, D.; Spiel, C.; Suchorski, Y.; Trinchero, A.; Schlögl, R.; Grönbeck, H.; Rupprechter, G. Local catalytic ignition during CO oxidation on low-index Pt and Pd Surfaces: A combined PEEM, MS, and DFT Study. *Angew. Chem., Int. Ed.* **2012**, *51*, 10041−10044.

(32) Fultz, B. Vibrational thermodynamics of materials. *Prog. Mater. Sci.* **2010**, *55*, 247−352.

(33) Eyring, H. The activated complex and the absolute rate of chemical reactions. *Chem. Rev.* **1935**, *17*, 65−77.

(34) Pingel, T. N.; Jørgensen, M.; Yankovich, A. B.; Grönbeck, H.; Olsson, E. Influence of atomic site-specific strain on catalytic activity of supported nanoparticles. *Nat. Commun.* **2018**, *9*, 2722.

(35) Bligaard, T.; Nørskov, J. K.; Dahl, S.; Matthiesen, J.; Christensen, C. H.; Sehested, J. The Brønsted−Evans−Polanyi relation and the volcano curve in heterogeneous catalysis. *J. Catal.* **2004**, *224*, 206−217.

(36) Jørgensen, M.; Grönbeck, H. Scaling relations and kinetic Monte Carlo simulations to bridge the materials gap in heterogeneous catalysis. *ACS Catal.* **2017**, *7*, 5054−5061.

(37) Bosio, N.; Grönbeck, H. Sensitivity of Monte Carlo Simulations to Linear Scaling Relations. *J. Phys. Chem. C* **2020**, *124*, 11952−11959.

(38) Falsig, H.; Hvolbæk, B.; Kristensen, I. S.; Jiang, T.; Bligaard, T.; Christensen, C. H.; Nørskov, J. K. Trends in the Catalytic CO Oxidation Activity of Nanoparticles. *Angew. Chem., Int. Ed.* **2008**, *47*, 4835−4839.

(39) Lee, J.; Ryou, Y.; Kim, J.; Chan, X.; Kim, T. J.; Kim, D. H. Influence of the Defect Concentration of Ceria on the Pt Dispersion and the CO Oxidation Activity of Pt/CeO_2. *J. Phys. Chem. C* **2018**, *122*, 4972−4983.

(40) Maurer, F.; Beck, A.; Jelic, J.; Wang, W.; Mangold, S.; Stehle, M.; Wang, D.; Dolcet, P.; Gänzler, A. M.; Kübel, C.; et al. Surface Noble Metal Concentration on Ceria as a Key Descriptor for Efficient Catalytic CO Oxidation. *ACS Catal.* **2022**, *12*, 2473−2486.

https://doi.org/10.1021/acs.jpcc.2c04833
J. Phys. Chem. C 2022, 126, 16164−16171